Steady-state phases and interaction-induced depletion in a driven-dissipative chirally-coupled dissimilar atomic array

Shao-Hong Chung [1,2,*] I Gusti Ngurah Yudi Handayana [3,4,2,*] Yi-Lin Tsao [2]
Chun-Chi Wu [2] G.-D. Lin [1,5,6] and H. H. Jen [2,3,5,†]

[1]*Department of Physics and Center for Quantum Science and Engineering, National Taiwan University, Taipei 10617, Taiwan*
[2]*Institute of Atomic and Molecular Sciences, Academia Sinica, Taipei 10617, Taiwan*
[3]*Molecular Science and Technology Program, Taiwan International Graduate Program, Academia Sinica, Taiwan*
[4]*Department of Physics, National Central University, Taoyuan City 320317, Taiwan*
[5]*Physics Division, National Center for Theoretical Sciences, Taipei 10617, Taiwan*
[6]*Trapped-Ion Quantum Computing Laboratory, Hon Hai Research Institute, Taipei 11492, Taiwan*

A nanophotonic waveguide coupled with an atomic array forms one of the strongly coupled quantum interfaces to showcase many fascinating collective features of quantum dynamics. In particular, for a dissimilar array of two different interparticle spacings with competing photon-mediated dipole-dipole interactions and directionality of couplings, we study the steady-state phases of atomic excitations under a weakly driven condition of laser field. We identify a partial set of steady-state phases of the driven system composed of combinations of steady-state solutions in a homogeneous array. We also reveal the intricate role of the atom at the interface of the dissimilar array in determining the steady-state phases and find an alteration in the dichotomy of the phases strongly associated with steady-state distributions with crystalline orders. We further investigate in detail the interaction-induced depletion in half of the dissimilar array, where the blockaded region results from two contrasting interparticle spacings near the reciprocal coupling regime. This can be further evidenced from the analytical solutions under the reciprocal coupling. Our results can provide insights in the driven-dissipative quantum phases of atomic excitations with nonreciprocal couplings and pave the avenues toward quantum simulations of exotic many-body states essential for quantum information applications.

I. INTRODUCTION

A driven-dissipative quantum system [1–7] provides unprecedented opportunities to explore nonequilibrium phase transitions [6] and to create strongly correlated steady states useful for quantum information processing [3]. This relies on an interplay or a competition between dissipations and interaction strengths, from which novel quantum many-body states and associated rich dynamical phenomena can emerge. Recently, an intriguing atom-waveguide QED platform [8–15], a distinct class of open quantum systems [16–24], showcased nontrivial collective radiations [25–34], long-range quantum correlations [35–39] owing to the strong couplings between atoms and the guided modes [40,41], and the tailored nonreciprocity [8,42–44] in the bidirectional couplings controlled via external magnetic fields.

This controlled and effective nonreciprocal coupling between atoms has been implemented in artificial quantum emitters [45–50], atom-nanofiber systems [19,41,42,51], and diamond nanophotonics platforms [52,53]. Within these strongly coupled systems, it is the photon-mediated and long-range dipole-dipole interaction [41] that leads to significant quantum correlations and allows many intriguing applications in routing or interfering photons, useful for integrated quantum network and scalable quantum computation [48]. An extra degree of freedom in manipulating the directionality of couplings [42] thus offers angles in studying quantum dynamics in these quantum interfaces and provides novel applications in quantum simulations or quantum computation in the next-generation nanophotonic devices.

Recent efforts focused on integrating dissimilar arrays with clean and disordered zones [54] or with disparate interparticle spacings [55,56]. The first intends to reveal the mechanism of many-body delocalization in the Bose-Hubbard model, while the second investigates the Anderson-like localization to delocalization transition and atomic excitation trapping effect. This dissimilar array is less explored especially under the driven-dissipative condition, where distinct steady-state phases can emerge with an interplay between the directionality of couplings and the strength of photon-mediated dipole-dipole interaction. Here we study the steady-state phases in a driven-dissipative dissimilar atomic array with

*These authors contributed equally to this work.
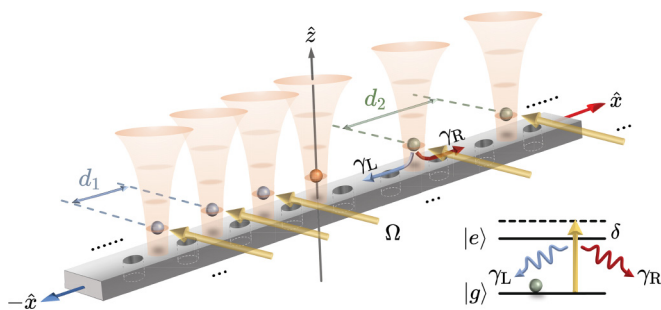†sappyjen@gmail.com

FIG. 1. Schematic illustration of weakly driven dissimilar chirally coupled atomic array. The system comprises two-level quantum emitters with effective nonreciprocal decay rates, $\gamma_L \neq \gamma_R$, which can be facilitated by the guided modes on a waveguide with external magnetic fields and is driven weakly by a uniform laser field with a Rabi frequency Ω and a detuning δ from a side excitation. There are two zones divided by dissimilar interatomic spacings $d_{1(2)}$, which, respectively, can be classified as two homogeneous atomic chains. An atom located at the interface of the dissimilar array is denoted as the interface atom with two disparate nearest-neighbor spacings. The inset plot shows the two-level quantum emitter with $|g\rangle$ and $|e\rangle$ indicating the ground and excited states, respectively.

chiral couplings, where a plethora of steady-state phases are uncovered with features resembling some of the steady-state phases in a homogeneous array. A competition between interparticle spacings and directionality of couplings further results in an interaction-induced depletion of atomic excitations, in huge contrast to the homogeneous array under a uniform and weak laser excitation. We investigate this unique steady-state phase with exploration of various parameters and locate the parameter region that supports the interaction-induced depletion feature, along with explanations from analytical calculations in the reciprocal coupling regime. Our findings can offer valuable insights into the driven-dissipative and interaction-induced quantum phases of atomic excitations with nonreciprocal couplings and open avenues for simulations of exotic quantum states useful for quantum information applications.

The paper is organized as follows. In Sec. II, we introduce the theoretical model of driven-dissipative dissimilar atomic array with two disparate interparticle spacings and nonreciprocal couplings. In Sec. III, we present the steady-state phases of atomic excitations. We further investigate the interaction-induced depletion in the dissimilar array in Sec. IV, where we identify the parameter regions that manifest the significant excitation depletion. Finally, we discuss and conclude in Sec. V.

II. THEORETICAL MODEL

We consider a weakly driven chirally-coupled atomic array consisting of atoms that are uniformly spaced at d_1 and d_2 in the left and right segments, respectively, as illustrated in Fig. 1. The atom located at the intersection of the two segments is termed the "interface atom," which bridges two segments with two different spacings $d_1 \neq d_2$. The motivation of considering a dissimilar array is to introduce an interplay of two distinct mechanisms of photon-mediated dipole-dipole interactions owing to two different interparticle distances, from

which we can reveal intriguing features of the steady states under weakly driven conditions. A straightforward experimental consideration is to use optical tweezer arrays to trap dissimilar atomic arrays, in such a way to realize our system setup with individual controls [10,20,22]. This dissimilar array can also be potentially realized in superconducting qubits systems or quantum dots in the waveguide platforms [8,15], where these quantum emitters can be placed in well-controlled positions by fabrication process.

The effective model of an atom-waveguide system can be obtained by treating the guided modes on a waveguide as a one-dimensional reservoir [35,44]. Within the interaction picture and under the Born-Markov approximation [57], the dynamical evolution of the system's density matrix ρ can be governed by

$$\frac{d\rho}{dt} = -\frac{i}{\hbar}[H_S + H_L + H_R, \rho] + \mathcal{L}_L[\rho] + \mathcal{L}_R[\rho], \quad (1)$$

with Hamiltonians H_S the light-matter interaction from a laser excitation, $H_{L(R)}$ the chiral couplings, and Lindblad forms of $\mathcal{L}_{L(R)}[\rho]$ indicating the chiral dissipations to the left (L) or the right (R) side of the waveguide. The Hamiltonian H_S is

$$H_S = \hbar \sum_{\mu=1}^{N} [\Omega e^{ikx_\mu \cos\theta}(\sigma_\mu + \sigma_\mu^\dagger) - \delta_\mu \sigma_\mu^\dagger \sigma_\mu], \quad (2)$$

which drives a collection of N two-level quantum emitters (characterized by the ground state $|g\rangle$ and the excited state $|e\rangle$) with a Rabi frequency Ω and spatially dependent detunings δ_j. The dipole raising and lowering operators are defined as $\sigma_\mu^\dagger \equiv |e\rangle_\mu \langle g|$ and $\sigma_\mu = (\sigma_\mu^\dagger)^\dagger$, respectively. $k = 2\pi/\lambda$ is the wave number with the transition wavelength λ, while the uniform excitation angle denoted as θ characterizes the propagation phases of the driving field from a lateral excitation away but close to the $\hat{x}$-$\hat{z}$ plane. The $H_{L(R)}$ are

$$H_{L(R)} = -i\hbar \frac{\gamma_{L(R)}}{2} \sum_{\mu<(>)\nu}^{N} (e^{ik|x_\mu - x_\nu|} \sigma_\mu^\dagger \sigma_\nu - \text{H.c.}), \quad (3)$$

which denote the collective energy shifts arising from the infinite-range photon-mediated dipole-dipole interaction [41]. The remaining dissipative parts in Lindblad forms are

$$\mathcal{L}_{L(R)}[\rho] = \gamma_{L(R)} \sum_{\mu,\nu=1}^{N} e^{\mp ik(x_\mu - x_\nu)} \left[\sigma_\nu \rho \sigma_\mu^\dagger - \frac{1}{2} \{\sigma_\mu^\dagger \sigma_\nu, \rho\} \right], \quad (4)$$

which describe the collective and nonreciprocal decay rates with $\gamma_L \neq \gamma_R$ in general. The directionality factor of the couplings can be quantified as $D \equiv (\gamma_R - \gamma_L)/\gamma$ [42] with $\gamma = \gamma_R + \gamma_L \equiv 2|dq(\omega)/d\omega|_{\omega=\omega_{eg}} g_k^2 L$ [35]. $|dq(\omega)/d\omega|$ indicates the inverse of group velocity at a resonant wave vector $q(\omega)$, with the atom-waveguide coupling strength g_k and the quantization length L.

We note that the Lindblad forms presented above neglect the nonguided decay γ_{ng} or additional nonradiative losses experienced by the atoms. This omission could potentially affect the efficiency of light detection through fibers, as well as the fidelity of the steady-state preparations. Typically, around 99% of light would be scattered in an atom-nanofiber system owing to the free-space decay [15]. The free-space decay

is intrinsic and is considered to be the same for all identical atoms. When the free-space decay dominates over the spin-exchange interactions mediated among the atoms, a homogeneous atomic excitation distribution will be observed, and the features of steady-state phases presented in this work will be removed. This demands a strong coupling regime which is more challenging for atom-nanofiber systems but can be facilitated in quantum dots or superconducting qubits systems. Later in Sec. III, we will discuss the steady-state phases under finite free-space decays, where γ_{ng} can be added into Eq. (1) as an extra intrinsic dissipation from environment or systematic uncertainties.

We can label the positions of atoms such that $x_\mu > x_\nu$ when $\mu > \nu$ for the array without loss of generality. To facilitate our analysis, we initialize the system in the ground state $|g\rangle^{\otimes N}$ and consider the system dynamics under a weak-field excitation. This results in a confined and self-consistent Hilbert subspace for dynamical evolutions within the ground state and singly excited states $\{|g\rangle^{\otimes N}, |\psi_\mu\rangle = |e\rangle_\mu |g\rangle^{\otimes (N-1)}\}$ for $\mu \in [1, N]$. This leads to the state representation

$$|\Psi(t)\rangle = \frac{1}{\sqrt{1 + \sum_{\mu=1}^{N} |p_\mu(t)|^2}} \left(|g\rangle^{\otimes N} + \sum_{\mu=1}^{N} p_\mu(t) |\psi_\mu\rangle \right),$$

(5)

where $p_\mu(t)$ represents the probability amplitude and $\sum_{\mu=1}^{N} |p_\mu(t)|^2 \ll 1$ to satisfy the assumption of a weak-field excitation.

Thus Eq. (1) can be reduced to a non-Hermitian Schrödinger equation $i\hbar\partial_t |\Psi(t)\rangle = H_{\text{eff}} |\Psi(t)\rangle$ with the effective Hamiltonian H_{eff}, yielding the coupled equations for $p_\mu(t)$ as

$$\dot{p}_\mu = -i\Omega e^{ikx_\mu \cos\theta} + \sum_{\nu=1}^{N} M_{\mu\nu} p_\nu,$$

(6)

where the matrix elements $M_{\mu\nu}$ of the coupling matrix M are

$$M_{\mu\nu} = \begin{cases} -\gamma_L e^{ik|x_\mu - x_\nu|}, & \mu < \nu, \\ i\delta_\mu - \frac{\gamma_L + \gamma_R}{2}, & \mu = \nu, \\ -\gamma_R e^{ik|x_\mu - x_\nu|}, & \mu > \nu. \end{cases}$$

(7)

Consequently, the probability amplitudes in the steady states $(\dot{p}_\mu = 0)$ are given by

$$\tilde{p}_\mu \equiv p_\mu(t \to \infty) = i\Omega \sum_{\nu=1}^{N} (M^{-1})_{\mu\nu} e^{ikx_\nu \cos\theta}.$$

(8)

For convenience, we define the interatomic distances as

$$k(x_\mu - x_{\mu-1}) = \begin{cases} kd_1 \equiv \xi_1, & 1 < \mu \leqslant m, \\ kd_2 \equiv \xi_2, & m < \mu \leqslant N, \end{cases}$$

(9)

where m denotes the index of the interface atom. From Eqs. (6) and (7), we are able to identify the interaction-driven quantum phases of atomic excitations, which are predominantly determined by the directionality of couplings D and photon-mediated dipole-dipole interactions. The interactions are decisively influenced by the interatomic separations. In the following section we proceed to characterize the composite

quantum phases that emerge from a homogeneous atomic array and discuss the interaction-induced depletion that is unique and only exists in certain parameter regimes.

We note that an alternative way to implement an effective dissimilar array is by illuminating two segments with two different excitation angles. This provides a straightforward setting to differentiate two segments by excitations, but this approach with two different Bragg angles would then focus on an interplay of the disparate imprinted traveling phases on the homogeneous atomic chain. This contrasts with our motivation of unveiling the effect of disparate photon-mediated dipole-dipole interactions and their interplay of interaction mechanisms in determining the steady-state phases. Some attempts of using Bragg configurations in an atom-waveguide systems have focused on the light scattering and light transmission through a waveguide [58] and the strongly-driven quantum dynamics of atoms [59]. We believe that significant interference effect resulting from two excitation angles with different imprinted traveling phases would be responsible for many other intriguing steady-state phases. This warrants further and future study along the direction of manipulating two excitation angles and on the many other distinct steady-state phases allowed in this setting.

III. STEADY-STATE PHASES

Here we obtain the steady-state phases in a weakly driven chirally-coupled dissimilar atomic array. Throughout the study, we locate the interface atom at the site of $m = \lceil N/2 \rceil$ with a ceiling function. Since D quantifies the degree of directional couplings and dissipations, we denote $D = 0$ as bidirectional and ± 1 as unidirectional coupling, respectively. We assume a perpendicular laser excitation at $\theta = \pi/2$ and uniform laser detunings $\delta_\mu = 0$. Under these conditions, we numerically calculate the normalized steady-state population distributions $\tilde{P}_j$ which are defined as

$$\tilde{P}_j = \frac{|\tilde{p}_j|^2}{\sum_{j=1}^{N} |\tilde{p}_j|^2}.$$

(10)

For the case of a homogeneous atomic array, we identified the steady-state phase diagram under the parameters of D and interparticle distance ξ [12]. In this weakly driven atomic array, the steady states can be characterized as the extended distributions (ETD) when $\xi \approx 0$, the phase with finite crystalline (CO) orders mostly for a finite D, the biedge excitations (BE) or the bihole excitations (BH) mostly for low D, and the chiral-flow dichotomy (CFD) when $\xi = \pi$. The ETD, CO, and BH phases present the delocalized characteristics, while the BE phase manifests localization properties, which can be distinguished by the participation ratio [60]. Meanwhile, the CO phase possesses an extra finite structure factor, while the BH phase shows hole excitations at the edges, which further differentiates the delocalized phases apart. The CFD phase resides at a very specific parameter of $\xi = \pi$ and shows two different population distributions depending on an odd or even N. This presents an interesting steady-state phase of the excited-state populations, where an extra number of atom gives rise to contrasted phases, and it resonates with the notion of "More is different" owing to the complexity and hierarchi-
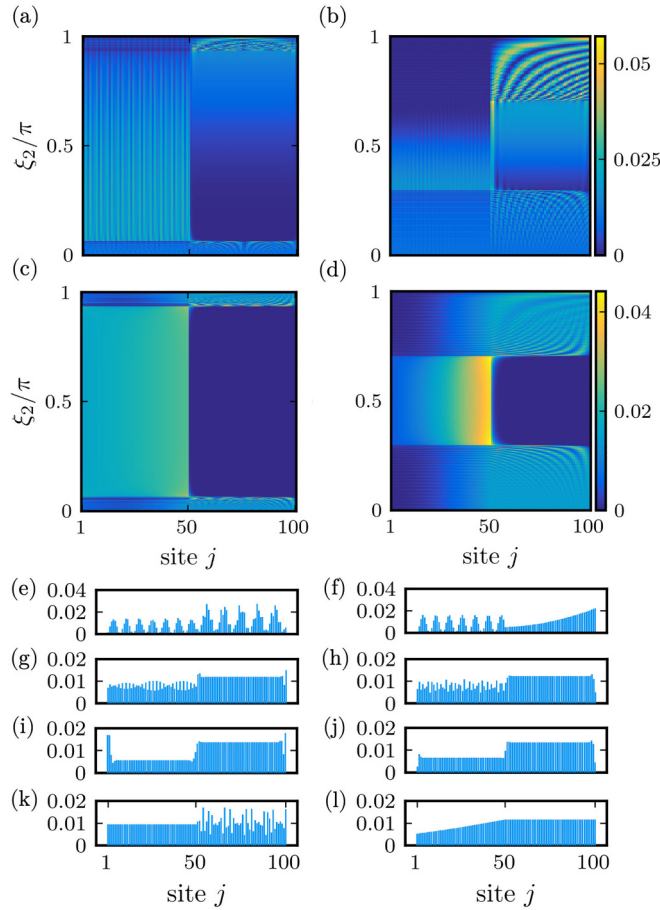
FIG. 2. The population distributions $\tilde{P}_j$ of the dissimilar array for $N = 100$ atoms. We illustrate $\tilde{P}_j$ with a dependence of ξ_2 at some chosen ξ_1 and D. In the panels (a)–(d), we set $\xi_1 = 0.02\pi$ in (a) and (b), and $\xi_1 = \pi$ in (c) and (d), while we choose $D = 0.2$ in (a) and (c), and $D = 0.8$ in (b) and (d), as comparisons. Some combinations of steady-state phases are demonstrated: (e) and (f) at $D = 0.5$ display CO-CO phase ($\xi_1 = 0.15\pi, \xi_2 = 0.9\pi$) and CO-CFD phase ($\xi_1 = 0.15\pi, \xi_2 = \pi$), respectively. Panel (g) depicts CO-BE phase ($D = 0.3, \xi_1 = 0.01\pi, \xi_2 = 0.3\pi$). Panel (h) illustrates CO-BH phase ($D = 0.5, \xi_1 = 0.1\pi, \xi_2 = 0.6\pi$). Panels (i), (j) at $D = 0.4$ feature BE-HE phase ($\xi_1 = 0.2\pi, \xi_2 = 0.3\pi$) and BH-BH phase ($\xi_1 = 0.6\pi, \xi_2 = 0.7\pi$), respectively. Panel (k) shows ETD-CO phase ($D = 0.6, \xi_1 = 2\pi, \xi_2 = 0.1\pi$). Finally, (l) presents CFD-ETD phase ($D = 0.2, \xi_1 = \pi, \xi_2 = 2\pi$).

cal structure in interacting quantum systems [61]. Two other critical parameter regimes of $D = 0$ and $\xi = \{0, \pi\}$ can also be identified and excluded from the steady-state phases owing to the constructive interference in state populations, a feature of decoherence-free space being populated predominantly and therefore leading to a breakdown under the weak-excitation assumption.

In Fig. 2, we present the excited-state population distributions in terms of parameter spaces ξ_1, ξ_2, and D. Based on the results of steady-state phases in a homogeneous array, in the setup of a dissimilar array we have 17 possible phases by accounting for the reflection symmetry in the system, which we discuss in detail in Appendix A. Interestingly, among these 17 steady states, we identify two extra configurations termed edge-hole (EH) or hole-edge (HE) excitations, which results from the influence of the interface atom and distinguishes from the previous BE or BH excitation phases in a homogeneous array. Figures 2(a) to 2(d) show some examples of cross sections in the three-dimensional parameters of ξ_1, ξ_2, and D. At a smaller ξ_1 in Figs. 2(a) and 2(b), the left segment hosts the CO phase, while in the right segment of the array, the steady-state phases transition from the ETD phase, the CO phase, to the BE excitation, the BH excitation phases, then the CO phase with interference patterns, and end up with the CFD phase as ξ_2 increases from 0 toward π. These six steady-state phases resemble parts of the features in a homogeneous array, and they can be seen clearly in either the left or the right segments of the array in Figs. 2(e) to 2(l). In Figs. 2(a) and 2(b), the dark-blue area in the right segment represents a low excited-state population in the bulk with the biedge excitations, while the light-blue area indicates a finite and flat distribution in the bulk, signifying the hole excitations at both the edges of the right segment.

Similarly in Figs. 2(c) and 2(d), the left segment of the array hosts the CFD phase with corresponding phase transitions in the right segment as ξ_2 increases as in Figs. 2(a) and 2(b). As D increases, we find the phase regions that host BE and BH excitations (dark and light blue regions in the right segment) are shrinking, which is expected and also appears in the case of homogeneous array [12], along with expanded phase areas of the CO phases (interference patterns) in Figs. 2(b) and 2(d). We note that the population distribution can exhibit significant differences in the respective total populations of the two segments, as demonstrated in Figs. 2(a) to 2(d), with this disparity becoming particularly pronounced when $\xi_1 = \pi$ in Figs. 2(c) and 2(d). This is why we see a seemingly flat distribution with low populations in the CO phase of the left segment in Fig. 2(b) (upper-left phase region). This manifests an intriguing steady-state phase with extremely low populations but still with the characteristics or the features of structure factors required in the CO phase. This low population can also be observed in the dark-blue areas in the right segment of Figs. 2(b) and 2(d), which we will study more in the next section. These extremely low-population phase areas showcase a surprisingly and notably blockaded region of atomic excitations. A thorough investigation of the mechanisms driving this phenomenon and its impact on the population distribution will be investigated in the next section.

In Figs. 2(e) to 2(l), we show the excited-state populations for some combinations of the steady-state phases. For example in Fig. 2(e), two CO phases can be identified with finite and peak values of the structure factors at two different periods of excitation oscillations. Specifically, regarding Fig. 2(i), the expectation from the insights of a homogeneous array suggests a BE-BE phase under the corresponding parameters. However, the numerical simulations reveal that it appears as the BE-HE phase instead, regardless of whether the interface atom is associated to the left or the right segment of the array. Similarly, when the number of atoms is odd (for example, of $N = 101$ with the interface atom at the site of $m = 51$) and under the same parameters in Fig. 2(i), BE-HE phase is also identified.

The CFD phase displayed in the left segment of Fig. 2(l) varies depending on the parity of the atom number in the
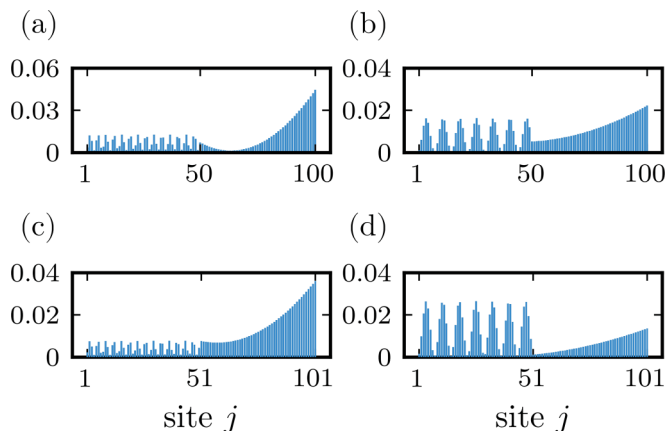
FIG. 3. Odd-numbered and even-numbered CFD phases in atomic chains with both odd and even total number of atoms. Panels (a) and (b) depict scenarios with a total even $N = 100$ atoms, where under the parameters of $D = 0.5$, $\xi_1 = 0.1\pi$, $\xi_2 = \pi$, and $D = 0.5$, $\xi_1 = 0.15\pi$, $\xi_2 = \pi$, respectively, odd-numbered and even-numbered CFD phases are observed in the right segment. Similarly, (c), (d) represent the cases for a total odd $N = 101$ atoms under the same parameter settings and demonstrate odd-numbered and even-numbered CFD phases in the right segment, respectively, as well.
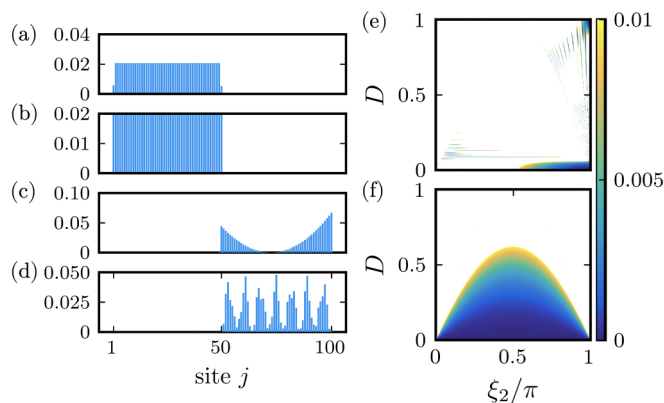

FIG. 4. The interaction-induced half-depletion (HF) phases for $N = 100$. (a) The BH-HD phase with mostly depleted BE in the right segment under the parameters $D = 0$, $\xi_1 = 0.8\pi$, and $\xi_2 = 0.02\pi$, with $B_D \approx 0.0013$. (b) The ETD-HD phase (depleted BE distribution in the right) for $D = 0.1$, $\xi_1 = 2\pi$, and $\xi_2 = 0.3\pi$, with $B_D \approx 0.0065$. (c) The HD-CFD phase (depleted hole-edge distributions in the left) for $D = 0.2$, $\xi_1 = 0.5\pi$, and $\xi_2 = \pi$, with $B_D \approx 0.0011$. (d) The HD-CO phase (depleted BE distribution in the left) for $D = 0.4$, $\xi_1 = 0.2\pi$, and $\xi_2 = 0.9\pi$, with $B_D \approx 0.0018$. Panels (e), (f) represent the half-depletion regimes under $B_D \leqslant 1/N$, with fixed parameters of $\xi_1 = 0.02\pi$ and $\xi_1 = \pi$.

left. When its atom number is even, the state in the CFD phase presents a linearly-increasing shape, as evidenced as well in Figs. 2(c) and 2(d) with a phase region when ξ_2 is around $\pi/2$. Conversely, with an odd number of atoms in the left under the same parameters, it would exhibit an upwardly concave curve instead as in the right segment in Fig. 2(f). This phenomenon is linked to the classification of the interface atom in which side of the atomic array. Intriguingly, even in cases with an even total number of atoms, an odd-numbered CFD can manifest and vice versa. Therefore, when $\xi_i = \pi$ for one segment in the CFD phase and $\xi_{j\neq i}$ on the other segment is chosen in the CO phase regime or near the boundary between the CO and the BE phases, this parameter regime triggers a sensitive alternation between even- and odd-numbered CFD phases as shown in Fig. 3. This can be seen in the distributions of the CFD phase in the left segment with striped patterns in Figs. 2(c) and 2(d), which are strongly associated with the CO phases in the right. This presents an intricate steady-state behaviors of the system owing to the interplay between the number of atoms in each segments and the photon-mediated spin-exchange couplings determined by interparticle spacings.

As for the effect of finite nonguided modes from free-space decay γ_{ng}, we compare the complete 17 phases between the cases of $\gamma_{\mathrm{ng}} = 0$ and $\gamma_{\mathrm{ng}}/\gamma = 0.01$ in Appendix A. We find that for a finite γ_{ng} that corresponds to almost 99% of the coupling into the waveguide, some features of the steady-state phases, for example, of ETD, CO, and CFD phases, are already influenced, and their overall profiles are either decreased or modified asymmetrically. Meanwhile, the BH and BE phases are kept intact and are robust to the free-space decay because they are originated from and strongly preserved in the reciprocal coupling regime of $D = 0$. Their features can be sustained down to around 50% of the light coupling. Nevertheless, an enhancement in the atom-waveguide coupling can

be achieved by introducing cavities into the atom-waveguide platforms for stronger confinement of light-matter couplings, where BE and BH phases can be much easier to be observed experimentally.

IV. INTERACTION-INDUCED DEPLETION

As shown in Figs. 2(c) and 2(d), we observe a significant decline of the excitation population in one segment. We term this unexpected phenomenon as the depletion phase. The occurrence of the phase depletion can be attributed to the complex spin-exchange interactions among the atomic array, arising from variations in interparticle spacings of the dissimilar array. In Figs. 4(a) to 4(d), we illustrate varied half-depletion patterns in the system. These diverse depletion phenomena in half of the atomic array underline an intricate interplay with competing parameters of long-range dipole-dipole interactions and directionality of couplings.

To systematically identify the parameter regimes that support this depletion phenomenon, we define a quantity of biased population (B_D) as a measure of the contrasted steady-state distributions between each segments of the dissimilar array

$$B_D \equiv 1 - \left| \frac{\sum_{\mu=1}^{m-1} \tilde{P}_\mu - \sum_{\mu=m+1}^{N} \tilde{P}_\mu}{\sum_{\mu=1}^{N} \tilde{P}_\mu - \tilde{P}_m} \right|, \qquad (11)$$

where we exclude the contribution from the interface atom at the mth site. As our discussion primarily focuses on the extent of overall population bias towards one side of the atomic array, this exclusion does not modify the conclusion from the analysis. From Eq. (11), B_D approaches one when a uniform distribution in the whole array is reached, while B_D becomes vanishing as a depleted region emerges. We then characterize
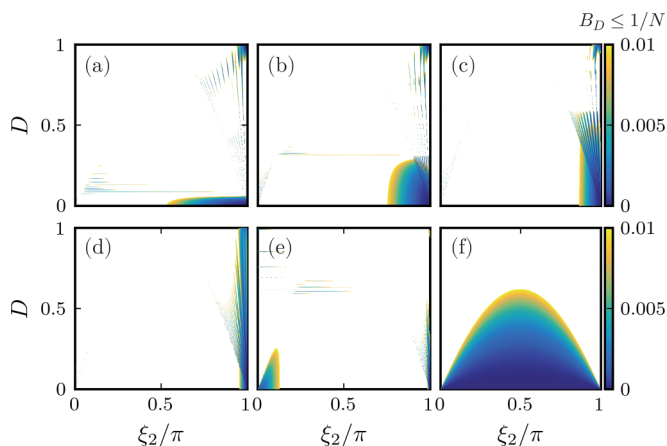
FIG. 5. Region of the half-depletion regime defined by $B_D \lesssim 1/N$ varies with different ξ_1. (a)–(f) illustrate the range of the half-depletion phases at $\xi_1 = 0.02\pi, 0.1\pi, 0.2\pi, 0.5\pi, 0.8\pi,$ and π, respectively. As ξ_1 gradually increases from small values close to $10^{-2}\pi$ to approximately $\pi/2$, the main concentration of the half-depletion region is observed on the right side of the diagram (i.e., in the interval where $\xi_2 \geqslant 0.5\pi$), transitioning from a wide and flat shape to a narrow and elongated form. Beyond $\pi/2$, the primary distribution of the half-depletion region begins to emerge on the left side (i.e., $\xi_2 \sim 0$), gradually expanding towards larger ξ_2 values, ultimately forming an arch-shaped structure as ξ_1 reaches π.
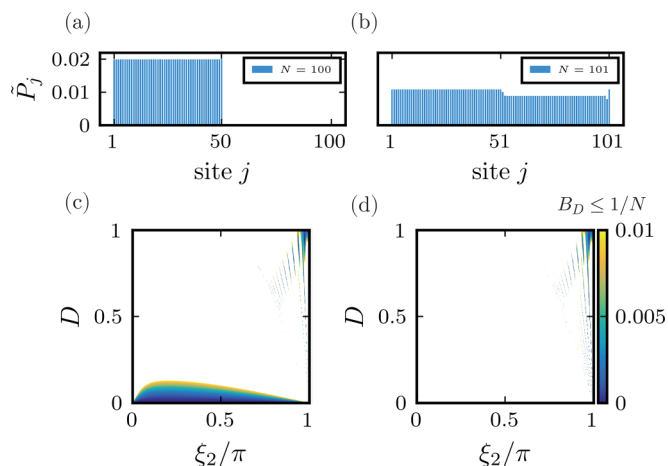

FIG. 6. The parity of the total number of atoms affects the half-depletion (HD) regime. Panels (a), (b) demonstrate the population distribution ($\tilde{P}_j$) for $N = 100$ and $N = 101$ under the same conditions $D = 0.1$, $\xi_1 = 2\pi$, and $\xi_2 = 0.3\pi$, revealing the subtle influence of the total atom number on the HD phase. Furthermore, (c), (d) illustrate the half-depletion parameter regimes for $N = 100$ and $N = 101$ at $\xi_1 = 2\pi$, where a finite range of HD phases exists at low D for even-numbered atomic systems.

the half-depletion (HD) phase in a dissimilar array if and only if $B_D \leqslant 1/N$. That is to say, the total population of the depleted side must be lower than a single-particle population on average, which sets a qualitative boundary for the HD phase.

In Figs. 4(e) and 4(f), we show the HD phase regime with two different ξ_1 for various ξ_2 and D under this criteria. A dominant parameter regime for the HD phase appears at a lower D for a small ξ_1 as shown in Fig. 4(e). As ξ_1 increases toward $\pi/2$ demonstrated in detail in Fig. 5, these parameter regions begin compressing towards a larger ξ_2 and extend along a higher D, which disappear as ξ_1 further increases but with new small regions of parameters emerging on the other side at small ξ_2. When ξ_1 reaches π, the HD phase boundary emerges with a parabola as seen in Fig. 4(f) covering most of the depletion phase area with almost all ξ_2 for a low D. This suggests that the depletion regime requires contrasted ξ_1 and ξ_2. Furthermore, in Fig. 6 we present the influence of the parity of the atomic number on HD phases. As in Fig. 3, the emergence of HD phases or not relies on the intricate interplay between the number of atoms and the photon-mediated dipole-dipole interactions. Other than the parameters chosen in Fig. 6, the HD phase regions are the same for even or odd N as ξ_1 and ξ_2 are away from 2π.

The depletion phase transition can be evidenced in the bidirectional case with $D = 0$ as shown in Figs. 7(a) and 7(b) with $\xi_1 = 0.02\pi$ and 0.2π, respectively. The measure B_D first rises as ξ_2 increases from 0 to approximately ξ_1, reaching near unity when $\xi_1 = \xi_2$, the case of a homogeneous array. As ξ_2 exceeds ξ_1 and increases further, B_D rapidly decreases and becomes vanishing toward $\xi_2 = \pi$. Additionally, as illustrated in Fig. 7(a), B_D decreases faster with increasing N, especially in the case of a small ξ_1. This leads to a diminishing

depletion region as N increases since the critical values of ξ_2 at which $B_D = 1/N$ increase, indicating a shrinking phase area for the HD phase. Below we further analyze the observation of shrinking phase area by providing analytical solutions in the
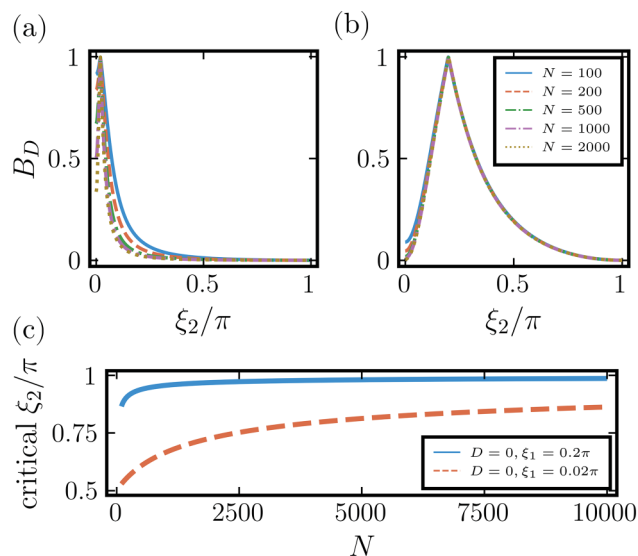

FIG. 7. Impact of system size on the depletion regime in the bidirectional ($D = 0$) case. The plots in (a) and (b) depict the dependence of B_D on ξ_2 at $\xi_1 = 0.02\pi$ and $\xi_1 = 0.2\pi$, respectively, for various atomic sizes $N = 100, 200, 500, 1000,$ and 2000. (c) illustrates a curve generated through Eq. (13) when equality holds, pinpointing the critical ξ_2, as it enters the half-depletion regime for system sizes ranging from $N = 100$ to $N = 10\,000$. Both scenarios of $\xi_1 = 0.02\pi$ (blue line) and $\xi_1 = 0.2\pi$ (orange dashed line) reveal that the depletion phase is a consequence of finite-size effect, which do not survive as $N \to \infty$.
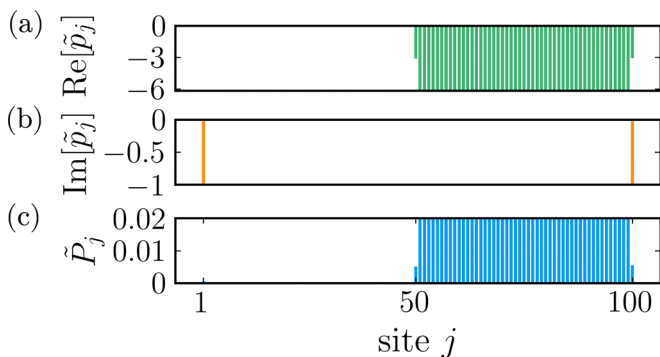
FIG. 8. The (a) imaginary and (b) real parts of the probability amplitudes $\tilde{p}_j$ for $N = 100$, $D = 0$, $\xi_1 = 0.02\pi$, and $\xi_2 = 0.8\pi$. The values are up to an overall constant of 2Ω. Panel (c) shows the normalized excited-state population $\tilde{P}_j$.

reciprocal coupling case of $D = 0$, which can give insights to the mechanism of the HD phase, and the obtained critical ξ_2 is plotted in Fig. 7(c) confirming the observations in numerical results in Figs. 7(a) and 7(b).

Under the bidirectional case of $D = 0$, that is $\gamma_R = \gamma_L$, we obtain the steady-state populations $\tilde{p}_\mu$ from Eq. (8) as

$$
\tilde{p}_\mu = -\Omega \times
\begin{cases}
i + \tan(\xi_1/2), & \mu = 1, \\
2\tan(\xi_1/2), & 1 < \mu < m, \\
\tan(\xi_1/2) + \tan(\xi_2/2), & \mu = m, \\
2\tan(\xi_2/2), & m < \mu < N, \\
i + \tan(\xi_2/2), & \mu = N,
\end{cases}
\tag{12}
$$

where the derivation is shown in detail in the Appendix B. A numerical calculation of $\tilde{p}_j$ for the parameters of $N = 100$, $D = 0$, $\xi_1 = 0.02\pi$, and $\xi_2 = 0.8\pi$ is plotted in Figs. 8(a) and 8(b), where the system hosts the HD phase as shown in Fig. 8(c). These results are consistent with the theoretical predictions in Eq. (12) in both real and imaginary parts.

From the measure B_D, we can analytically determine at which parameters the HD phase boundary locates. Considering an even N with the interface atom at the site $m = N/2$, as in the numerical simulations shown in Figs. 7(a), 7(b), and for a small ξ_1 as in Fig. 4(e), we obtain the range of ξ_2 when the HD phase emerges from Eq. (B8)

$$
\tan^2\left(\frac{\xi_2}{2}\right) \geqslant \frac{\left(N^2 - 2N + \frac{7}{4}\right)\tan^2(\xi_1/2) + \frac{N-1}{2}}{\frac{N}{2} - \frac{3}{4}}.
\tag{13}
$$

The phenomenon of depletion in the bi-directional cases straightforwardly occurs when $\tan^2(\xi_2/2)/\tan^2(\xi_1/2) \gtrsim 2N \gg 1$ (depleted from left side) or $\ll 1$ (depleted from right side) when $\xi_1 \leftrightarrow \xi_2$ for a large N. This relation indicates a drastic difference between ξ_1 and ξ_2, which allows the HD phase under the criteria of $B_D \leqslant 1/N$. This coincides with a relatively large critical ξ_2 at the HD phase boundary in Figs. 4 and 7, respectively, for a low D. The asymptotic function of Eq. (13) at equality is plotted in Fig. 7(c), where the numerically obtained critical ξ_2 are on top with these curves. This indicates the phase boundary $\xi_2 \to \pi$ as $N \to \infty$ and manifests an ultimately vanishing depletion region. This also suggests that the depletion phenomenon under our restricted

criteria results from the finite-size effect, except for the case of $\xi_1 = \pi$ where all ξ_2 with a finite region of D allow the existence of HD phase as shown in Fig. 4(f). As the criteria relaxes to the two-particle population on average, for example, or more but finite, the phase areas of the HD phase would expand and the fate of this phase in the thermodynamics limit could survive.

V. DISCUSSION AND CONCLUSION

The study of atomic dissimilar array coupled to a nanophotonic waveguide under a weakly-driven condition provides one of the unique driven-dissipative quantum systems that can host many fascinating nonequilibrium dynamics and steady-state phases. This is due to an intricate interplay between various competing parameters of long-range dipole-dipole interactions and the directionality of couplings. Our investigation of such system reveals the essential combinations of steady-state phases from a homogeneous array, where new state configurations like a hole with an edge excitation at the interface and the edge, respectively, can emerge. In addition, the interface atom that bridges two segments with different interparticle spacings presents an intriguing role in deciding and characterizing the steady-state phases. Another intriguing and significant result is the apparent decline in state populations in one of the two segments, indicating a blockaded region of atomic excitations. This effect arises from the contrasted interparticle spacings in the dissimilar array near the reciprocal coupling regime, which we attribute as the interaction-induced half-depletion phase. Our results can provide insights to quantum engineering or quantum simulations of exotic many-body states with high controllability.

The decrease in population distribution inside one of the segments has significant implications for quantum information processing. The depletion phase predicted in a specific segment adds to the complexity of the quantum state by introducing more degrees of freedom for encoding quantum information. This can be done in designing distinct arrangement of atoms, particularly when separated into two regions. The disparity in the interparticle distances between atoms then serves as a means to encode and manipulate quantum information in these states. For example, a single photon can go through a beam splitter and interact with two settings of dissimilar atomic arrays with either the left or the right segment hosts a depleted region. This leads to an entangled state of $|0_L 1_R\rangle + |1_L 0_R\rangle$ in terms of vanishing or occupied qubit states by constructing the entangling degrees of freedom in segmented spaces. The two settings of dissimilar atomic arrays interacting with path-entangled single photon is no difference from an entanglement generation from single photon going through a beam splitter. This entanglement generation is associated with the concept of single-particle entanglement [62], where a genuine entanglement can be created from a single photon going through a 50 : 50 beam splitter with an outcome of two possible modes (transmitted as mode A or reflected as mode B). This leads to an entangled state $|0_A 1_B\rangle + |1_A 0_B\rangle$ which possesses a maximally bipartite entanglement entropy, and this also provides the foundation for entanglement generation in the well-known DLCZ protocol under a weak-field excitation with two atomic ensembles [63].

The outlook for potential quantum information processing using our proposed setup with interaction-induced depletion phases is simply a transfer of path-entangled single-photon state to spatially entangled atomic segments. Based on the design of using two segmented qubits to generate a bipartite entangled state, we can consider a unit of two segments concatenated by a series of separate and homogeneously arrayed qubits to form a scalable W state. If we follow the convention of denoting $|0\rangle$ as the depleted state, we can generate a W state in a form of $(|\underline{011}\cdots 1\rangle + |1\underline{011}\cdots 1\rangle + \cdots + |1\cdots 1\underline{01}\rangle + |1\cdots 1\underline{10}\rangle)$, where an underlined unit denotes the two segments with depletion either in the left or the right of the dissimilar arrays. This W state is equivalent to $(|10\cdots 0\rangle + |010\cdots 0\rangle + \cdots + |0\cdots 01\rangle)$ up to single-qubit rotations on each qubit spaces individually by mapping $|0\rangle \leftrightarrow |1\rangle$. We note that this maximally entangled state as a W type can be generated when we multiplex a weak field source in a way that all concatenated configurations with a unit of two segments are identically excited. This promises a high-capacity entanglement generation and simulation of exotic quantum many-body states in spatial degrees of freedom. The application of manipulating dissimilar atomic array thus promises many other opportunities in routing photons [56], allowing parallel quantum operations [64], or creating multipartite entangled states [65].

As a final remark, we note that a more viable platform to carry out our proposal and results here would be using photonic crystal waveguides instead of nanofibers. In atom-nanofiber systems, the challenges to reach the strong coupling regime comes from significant free-space scattering and thermal vibrations of the fibers, which leads to an issue of trapping atoms close to the fibers. Meanwhile, atom-nanophotonic waveguides as shown in Fig. 1, superconducting transmon qubits, silicon vacancies in diamonds, and quantum dots are better candidates for experimental realizations in terms of achieving strong coupling regime [15]. For atom-waveguide systems in general, it is still challenging to overcome position fluctuations of atoms [10], and this detrimental effect can be lessened by Raman sideband cooling to reduce motional fluctuations of atoms in optical tweezers [66] or applying gray-molasses loading to optical tweezers [67].

APPENDIX A: COMPLETE SET OF STEADY-STATE PHASES IN A DISSIMILAR ARRAY

Here we show the probability distributions for the complete 17 steady-state phases in a dissimilar array. As shown in Fig. 9, we observe various combinations of steady-state phases in a homogeneous array. Other than these combinations, we have extra phases that a homogeneous array does not host, which are EH and HE configurations. Furthermore, we obtain the half-depletion phases that show extremely low state populations as shown in Figs. 9(l), 9(m), 9(n), 9(p), and 9(q).
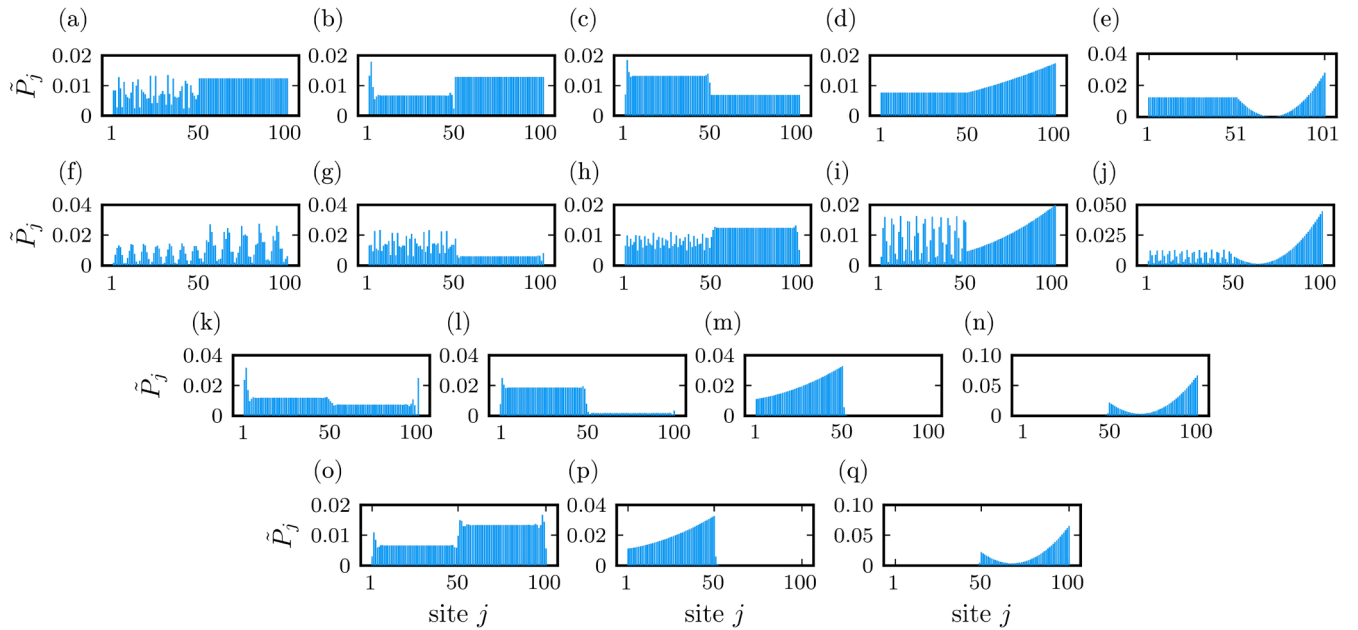

FIG. 9. Excited-state distributions $\tilde{P}_j$ for 17 steady-state phases in a dissimilar array. These phases include (a) CO-ETD, (b) BE-ETD, (c) BH-ETD, (d) ETD with even-numbered CFD, (e) ETD with odd-numbered CFD specifically at $N = 101$, (f) CO-CO, (g) CO-BE, (h) CO-BH, (i) CO with even-numbered CFD, (j) CO with odd-numbered CFD, (k) EH-HE (overall BE), (l) BH-BE, (m) even-numbered CFD with depleted BE (dBE), (n) dBE with odd-numbered CFD, (o) BH-BH, (p) even-numbered CFD with depleted EH (dEH), (q) depleted HE (dHE) with odd-numbered CFD. All phases are presented at $N = 100$ except for (e) at $N = 101$. The parameters for each panel are detailed in Table I.

TABLE I. Parameter D, ξ_1, and ξ_2 for 17 phases.

Fig. 9	Steady-state phases	D	ξ_1/π	ξ_2/π
(a)	CO-ETD	0.5	0.1	2
(b)	BE-ETD	0.5	0.25	2
(c)	BH-ETD	0.5	0.5	2
(d)	ETD-eCFD	0.2	2	1
(e)	ETD-oCFD	0.2	2	1
(f)	CO-CO	0.5	0.15	0.9
(g)	CO-BE	0.5	0.1	0.3
(h)	CO-BH	0.5	0.1	0.6
(i)	CO-eCFD	0.4	0.1	1
(j)	CO-oCFD	0.5	0.1	1
(k)	EH-BE	0.5	0.25	0.2
(l)	BH-BE	0.5	0.6	0.25
(m)	eCFD-dBE	0.5	1	0.25
(n)	dBE-oCFD	0.5	0.25	1
(o)	BH-BH	0.7	0.6	0.7
(p)	eCFD-dEH	0.5	1	0.75
(q)	dHE-oCFD	0.5	0.75	1

We note that there is no ETD-ETD phase since it becomes the ETD phase exactly as in a homogeneous array. There are also no allowed combinations with either even-numbered CFD (eCFD) or odd-numbered CFD (oCFD) phases since they hugely depend on the boundary effect from the parity of the atom numbers. By contrast, the CO-CO or the BH-BH phases can emerge owing to the disparity of respective state populations of two segments, which distinguishes the case in a homogeneous array. In Fig. 10, we add the nonguided decay rate γ_{ng} from free-space decay which scatters light without coupling to the waveguide. As a comparison to Fig. 9,

the ETD, CO, and CFD phases in one of the two dissimilar segments are mostly influenced by γ_{ng}, whereas the BH and BE phases are kept intact and relatively robust to a finite γ_{ng}.

APPENDIX B: DERIVATION OF EXCITED-STATE PROBABILITY AMPLITUDES

Here we provide some details of the derivation of the excited-state probability amplitudes. We first consider the homogeneous array with identical interparticle spacings. We consider the laser incident angle $\theta = \pi/2$ and detuning $\delta_\mu = 0$, and we obtain the coupling matrix as (normalized to γ),

$$M_{\mu\nu} = -\frac{1}{2} \times \begin{cases} (1-D)e^{i\xi|\nu-\mu|}, & \mu < \nu, \\ 1, & \mu = \nu, \\ (1+D)e^{i\xi|\mu-\nu|}, & \mu > \nu. \end{cases} \quad \text{(B1)}$$

The inverse of M in the bidirectional coupling case can then be obtained as

$$(M^{-1})_{\mu\nu} = \frac{-2}{1-e^{2i\xi}} \times \begin{cases} 1, & \mu = \nu = 1 \text{ or } N, \\ 1+e^{2i\xi}, & 1 < \mu = \nu < N, \\ -e^{i\xi}, & |\mu-\nu| = 1, \\ 0, & \text{otherwise}, \end{cases} \quad \text{(B2)}$$

and from Eq. (6), we obtain the steady-state solutions of the dissimilar array

$$\tilde{p}_\mu = -\Omega \times \begin{cases} i + \tan(\xi_1/2), & \mu = 1 \text{ or } N, \\ 2\tan(\xi/2), & 1 < \mu < N. \end{cases} \quad \text{(B3)}$$

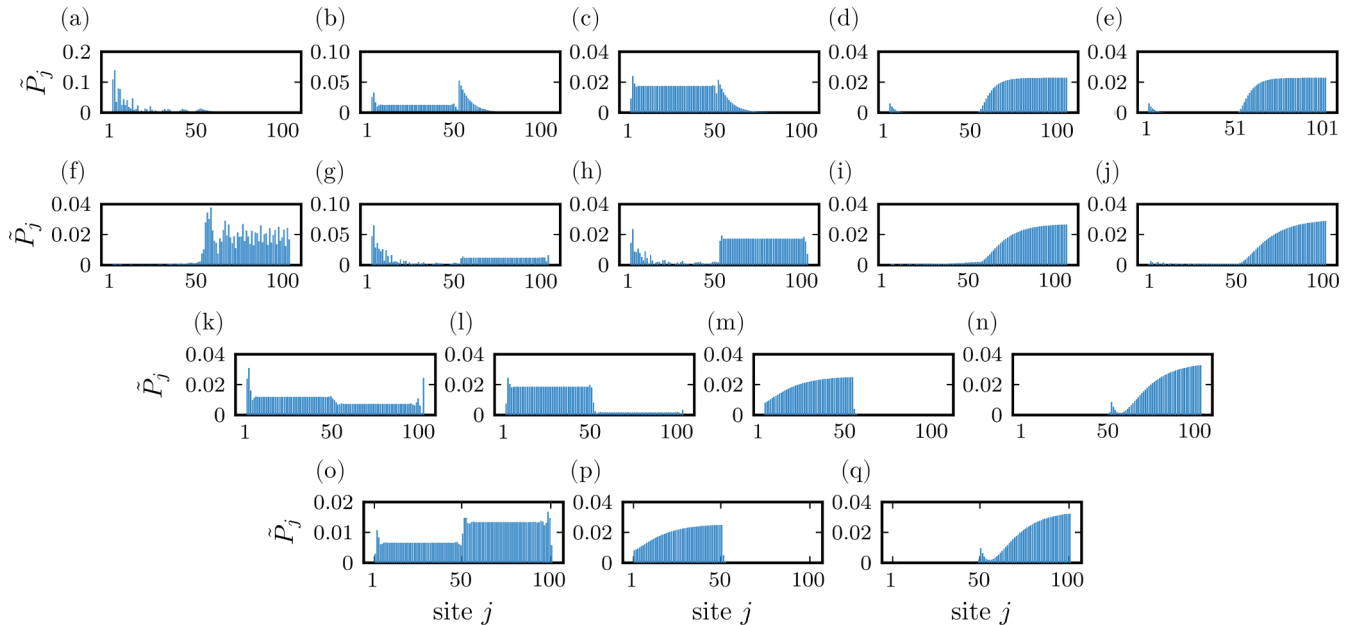

FIG. 10. Excited-state distributions $\tilde{P}_j$ for 17 steady-state phases in a dissimilar array at a finite free-space decay rate $\gamma_{ng}/\gamma = 0.01$. The rest of the parameters are the same as in Fig. 9.

Similarly, for the case of a dissimilar array, the coupling matrix M when $D = 0$ can be given as

$$
M_{\mu\nu} = -\frac{1}{2} \times
\begin{cases}
e^{i\xi_1|\nu-\mu|}, & \mu < \nu \leqslant m, \\
e^{i\xi_1|m-\mu|+i\xi_2|\nu-m|}, & \mu < m < \nu, \\
e^{i\xi_2|\nu-\mu|}, & m \leqslant \mu < \nu, \\
1, & \mu = \nu, \\
e^{i\xi_1|\nu-\mu|}, & m \geqslant \mu > \nu, \\
e^{i\xi_1|m-\nu|+i\xi_2|\mu-m|}, & \mu > m > \nu, \\
e^{i\xi_2|\mu-\nu|}, & \mu > \nu \geqslant m.
\end{cases}
\tag{B4}
$$

The inverse matrix M^{-1} can therefore be written as

$$
M^{-1} = -2 \times
\begin{bmatrix}
\frac{1}{1-e^{2i\xi_1}} & \frac{-e^{i\xi_1}}{1-e^{2i\xi_1}} & 0 & \cdots & \cdots & \cdots & \cdots & \cdots & 0 \\
\frac{-e^{i\xi_1}}{1-e^{2i\xi_1}} & \frac{1+e^{2i\xi_1}}{1-e^{2i\xi_1}} & \frac{-e^{i\xi_1}}{1-e^{2i\xi_1}} & 0 & \cdots & \cdots & \cdots & \cdots & 0 \\
0 & \frac{-e^{i\xi_1}}{1-e^{2i\xi_1}} & \ddots & \ddots & 0 & \cdots & \cdots & \cdots & 0 \\
\vdots & 0 & \ddots & \frac{1+e^{2i\xi_1}}{1-e^{2i\xi_1}} & \frac{-e^{i\xi_1}}{1-e^{2i\xi_1}} & 0 & \cdots & \cdots & 0 \\
\vdots & \vdots & 0 & \frac{-e^{i\xi_1}}{1-e^{2i\xi_1}} & \frac{1-e^{2i(\xi_1+\xi_2)}}{(1-e^{2i\xi_1})(1-e^{2i\xi_2})} & \frac{-e^{i\xi_2}}{1-e^{2i\xi_2}} & 0 & \cdots & 0 \\
\vdots & \vdots & \vdots & 0 & \frac{-e^{i\xi_2}}{1-e^{2i\xi_2}} & \frac{1+e^{2i\xi_2}}{1-e^{2i\xi_2}} & \frac{-e^{i\xi_2}}{1-e^{2i\xi_2}} & \ddots & \vdots \\
\vdots & \vdots & \vdots & \vdots & 0 & \frac{-e^{i\xi_2}}{1-e^{2i\xi_2}} & \ddots & \ddots & 0 \\
\vdots & \vdots & \vdots & \vdots & \vdots & \ddots & \ddots & \frac{1+e^{2i\xi_2}}{1-e^{2i\xi_2}} & \frac{-e^{i\xi_2}}{1-e^{2i\xi_2}} \\
0 & 0 & 0 & 0 & 0 & 0 & 0 & \frac{-e^{i\xi_2}}{1-e^{2i\xi_2}} & \frac{1}{1-e^{2i\xi_2}}
\end{bmatrix}.
\tag{B5}
$$

By solving the inverse matrix of M, we have the probability amplitudes $\tilde{p}_\mu$,

$$
\tilde{p}_\mu = -\Omega \times
\begin{cases}
i + \tan(\xi_1/2), & \mu = 1, \\
2\tan(\xi_1/2), & 1 < \mu < m, \\
\tan(\xi_1/2) + \tan(\xi_2/2), & \mu = m, \\
2\tan(\xi_2/2), & m < \mu < N, \\
i + \tan(\xi_2/2), & \mu = N,
\end{cases}
\tag{B6}
$$

where the cases for $\xi_{1,2} = 0$ or π should be excluded for divergence and a breakdown under the weak-field excitation. Therefore, we obtain the biased population B_D as

$$
1 - \left| \frac{\left(m - \frac{7}{4}\right)\tan^2\left(\frac{\xi_1}{2}\right) - \left(N - m - \frac{3}{4}\right)\tan^2\left(\frac{\xi_2}{2}\right)}{\frac{1}{2} + \left(m - \frac{7}{4}\right)\tan^2\left(\frac{\xi_1}{2}\right) + \left(N - m - \frac{3}{4}\right)\tan^2\left(\frac{\xi_2}{2}\right)} \right|.
\tag{B7}
$$

With an even N and $m = N/2$, the B_D becomes

$$
B_D = 1 - \left| \frac{\left(\frac{N}{2} - \frac{7}{4}\right)\tan^2\left(\frac{\xi_1}{2}\right) - \left(\frac{N}{2} - \frac{3}{4}\right)\tan^2\left(\frac{\xi_2}{2}\right)}{\frac{1}{2} + \left(\frac{N}{2} - \frac{7}{4}\right)\tan^2\left(\frac{\xi_1}{2}\right) + \left(\frac{N}{2} - \frac{3}{4}\right)\tan^2\left(\frac{\xi_2}{2}\right)} \right|.
\tag{B8}
$$

The above result can then be used to identify the phase boundary to the half-depletion phase in the main paper.

[1] S. Diehl, A. Micheli, A. Kantian, B. Kraus, H. P. Büchler, and P. Zoller, Quantum states and phases in driven open quantum systems with cold atoms, Nat. Phys. **4**, 878 (2008).

[2] B. Kraus, H. P. Büchler, S. Diehl, A. Kantian, A. Micheli, and P. Zoller, Preparation of entangled states by quantum Markov processes, Phys. Rev. A **78**, 042307 (2008).

[3] F. Verstraete, M. M. Wolf, and J. I. Cirac, Quantum computation and quantum-state engineering driven by dissipation, Nat. Phys. **5**, 633 (2009).

[4] K. Baumann, C. Guerlin, F. Brennecke, and T. Esslinger, Dicke quantum phase transition with a superfluid gas in an optical cavity, Nature (London) **464**, 1301 (2010).

[5] H. Weimer, M. Müller, I. Lesanovsky, P. Zoller, and H. P. Büchler, A Rydberg quantum simulator, Nat. Phys. **6**, 382 (2010).

[6] S. Diehl, A. Tomadin, A. Micheli, R. Fazio, and P. Zoller, Dynamical phase transitions and instabilities in open atomic many-body systems, Phys. Rev. Lett. **105**, 015702 (2010).

[7] J. T. Barreiro, M. Müller, P. Schindler, D. Nigg, T. Monz, M. Chwalla, M. Hennrich, C. F. Roos, P. Zoller, and R. Blatt, An open-system quantum simulator with trapped ions, Nature (London) **470**, 486 (2011).

[8] P. Lodahl, S. Mahmoodian, S. Stobbe, A. Rauschenbeutel, P. Schneeweiss, J. Volz, H. Pichler, and P. Zoller, Chiral quantum optics, Nature (London) **541**, 473 (2017).

[9] D. E. Chang, J. S. Douglas, A. González-Tudela, C.-L. Hung, and H. J. Kimble, *Colloquium:* Quantum matter built from nanoscopic lattices of atoms and photons, Rev. Mod. Phys. **90**, 031002 (2018).

[10] P. Samutpraphoot, T. Dordević, P. L. Ocola, H. Bernien, C. Senko, V. Vuletić, and M. D. Lukin, Strong coupling of two individually controlled atoms via a nanophotonic cavity, Phys. Rev. Lett. **124**, 063602 (2020).

[11] S. J. Masson and A. Asenjo-Garcia, Atomic-waveguide quantum electrodynamics, Phys. Rev. Res. **2**, 043213 (2020).

[12] H. H. Jen, Steady-state phase diagram of a weakly driven chiral-coupled atomic chain, Phys. Rev. Res. **2**, 013097 (2020).

[13] N. Fayard, L. Henriet, A. Asenjo-Garcia, and D. E. Chang, Many-body localization in waveguide quantum electrodynamics, Phys. Rev. Res. **3**, 033233 (2021).

[14] E. Kim, X. Zhang, V. S. Ferreira, J. Banker, J. K. Iverson, A. Sipahigil, M. Bello, A. González-Tudela, M. Mirhosseini, and O. Painter, Quantum electrodynamics in a topological waveguide, Phys. Rev. X **11**, 011015 (2021).

[15] A. S. Sheremet, M. I. Petrov, I. V. Iorsh, A. V. Poshakinskiy, and A. N. Poddubny, Waveguide quantum electrodynamics: Collective radiance and photon-photon correlations, Rev. Mod. Phys. **95**, 015002 (2023).

[16] E. Vetsch, D. Reitz, G. Sagué, R. Schmidt, S. T. Dawkins, and A. Rauschenbeutel, Optical interface created by laser-cooled atoms trapped in the evanescent field surrounding an optical nanofiber, Phys. Rev. Lett. **104**, 203603 (2010).

[17] J. D. Thompson, T. G. Tiecke, N. P. de Leon, J. Feist, A. V. Akimov, M. Gullans, A. S. Zibrov, V. Vuletić, and M. D. Lukin, Coupling a single trapped atom to a nanoscale optical cavity, Science **340**, 1202 (2013).

[18] A. Goban, C.-L. Hung, J. D. Hood, S.-P. Yu, J. A. Muniz, O. Painter, and H. J. Kimble, Superradiance for atoms trapped along a photonic crystal waveguide, Phys. Rev. Lett. **115**, 063601 (2015).

[19] N. V. Corzo, J. Raskop, A. Chandra, A. S. Sheremet, B. Gouraud, and J. Laurat, Waveguide-coupled single collective excitation of atomic arrays, Nature (London) **566**, 359 (2019).

[20] M. E. Kim, T.-H. Chang, B. M. Fields, C.-A. Chen, and C.-L. Hung, Trapping single atoms on a nanophotonic circuit with configurable tweezer lattices, Nat. Commun. **10**, 1647 (2019).

[21] H. H. Jen, Disorder-assisted excitation localization in chirally coupled quantum emitters, Phys. Rev. A **102**, 043525 (2020).

[22] T. Đorđević, P. Samutpraphoot, P. L. Ocola, H. Bernien, B. Grinkemeyer, I. Dimitrova, V. Vuletić, and M. D. Lukin, Entanglement transport and a nanophotonic interface for atoms in optical tweezers, Science **373**, 1511 (2021).

[23] O. A. Iversen and T. Pohl, Self-ordering of individual photons in waveguide QED and Rydberg-atom arrays, Phys. Rev. Res. **4**, 023002 (2022).

[24] G. Fedorovich, D. Kornovan, A. Poddubny, and M. Petrov, Chirality-driven delocalization in disordered waveguide-coupled quantum arrays, Phys. Rev. A **106**, 043723 (2022).

[25] L. Henriet, J. S. Douglas, D. E. Chang, and A. Albrecht, Critical open-system dynamics in a one-dimensional optical-lattice clock, Phys. Rev. A **99**, 023802 (2019).

[26] Y.-X. Zhang and K. Mølmer, Theory of subradiant states of a one-dimensional two-level atom chain, Phys. Rev. Lett. **122**, 203605 (2019).

[27] Y. Ke, A. V. Poshakinskiy, C. Lee, Y. S. Kivshar, and A. N. Poddubny, Inelastic scattering of photon pairs in qubit arrays with subradiant states, Phys. Rev. Lett. **123**, 253601 (2019).

[28] A. Albrecht, L. Henriet, A. Asenjo-Garcia, P. B. Dieterle, O. Painter, and D. E. Chang, Subradiant states of quantum bits coupled to a one-dimensional waveguide, New J. Phys. **21**, 025003 (2019).

[29] J. A. Needham, I. Lesanovsky, and B. Olmos, Subradiance-protected excitation transport, New J. Phys. **21**, 073061 (2019).

[30] H. H. Jen, M.-S. Chang, G.-D. Lin, and Y.-C. Chen, Subradiance dynamics in a singly excited chirally coupled atomic chain, Phys. Rev. A **101**, 023830 (2020).

[31] S. Mahmoodian, G. Calajó, D. E. Chang, K. Hammerer, and A. S. Sørensen, Dynamics of many-body photon bound states in chiral waveguide QED, Phys. Rev. X **10**, 031011 (2020).

[32] H. H. Jen, Bound and subradiant multiatom excitations in an atomic array with nonreciprocal couplings, Phys. Rev. A **103**, 063711 (2021).

[33] R. Pennetta, M. Blaha, A. Johnson, D. Lechner, P. Schneeweiss, J. Volz, and A. Rauschenbeutel, Collective radiative dynamics of an ensemble of cold atoms coupled to an optical waveguide, Phys. Rev. Lett. **128**, 073601 (2022).

[34] R. Pennetta, D. Lechner, M. Blaha, A. Rauschenbeutel, P. Schneeweiss, and J. Volz, Observation of coherent coupling between super- and subradiant states of an ensemble of cold atoms collectively coupled to a single propagating optical mode, Phys. Rev. Lett. **128**, 203601 (2022).

[35] A. González-Tudela and D. Porras, Mesoscopic entanglement induced by spontaneous emission in solid-state quantum optics, Phys. Rev. Lett. **110**, 080502 (2013).

[36] S. Mahmoodian, M. Čepulkovskis, S. Das, P. Lodahl, K. Hammerer, and A. S. Sørensen, Strongly correlated photon transport in waveguide quantum electrodynamics with weakly coupled emitters, Phys. Rev. Lett. **121**, 143601 (2018).

[37] C. A. Downing, J. C. López Carreño, A. I. Fernández-Domínguez, and E. del Valle, Asymmetric coupling between two quantum emitters, Phys. Rev. A **102**, 013723 (2020).

[38] H. Le Jeannic, T. Ramos, S. F. Simonsen, T. Pregnolato, Z. Liu, R. Schott, A. D. Wieck, A. Ludwig, N. Rotenberg, J. J. García-Ripoll, and P. Lodahl, Experimental reconstruction of the few-photon nonlinear scattering matrix from a single quantum dot in a nanophotonic waveguide, Phys. Rev. Lett. **126**, 023603 (2021).

[39] H. H. Jen, Quantum correlations of localized atomic excitations in a disordered atomic chain, Phys. Rev. A **105**, 023717 (2022).

[40] J. S. Douglas, H. Habibian, C.-L. Hung, A. V. Gorshkov, H. J. Kimble, and D. E. Chang, Quantum many-body models with cold atoms coupled to photonic crystals, Nat. Photon. **9**, 326 (2015).

[41] P. Solano, P. Barberis-Blostein, F. K. Fatemi, L. A. Orozco, and S. L. Rolston, Super-radiance reveals infinite-range dipole interactions through a nanofiber, Nat. Commun. **8**, 1857 (2017).

[42] R. Mitsch, C. Sayrin, B. Albrecht, P. Schneeweiss, and A. Rauschenbeutel, Quantum state-controlled directional spontaneous emission of photons into a nanophotonic waveguide, Nat. Commun. **5**, 5713 (2014).

[43] T. Ramos, H. Pichler, A. J. Daley, and P. Zoller, Quantum spin dimers from chiral dissipation in cold-atom chains, Phys. Rev. Lett. **113**, 237203 (2014).

[44] H. Pichler, T. Ramos, A. J. Daley, and P. Zoller, Quantum optics of chiral spin networks, Phys. Rev. A **91**, 042116 (2015).

[45] I. J. Luxmoore, N. A. Wasley, A. J. Ramsay, A. C. T. Thijssen, R. Oulton, M. Hugues, S. Kasture, V. G. Achanta, A. M. Fox, and M. S. Skolnick, Interfacing spins in an InGaAs quantum dot to a semiconductor waveguide circuit using emitted photons, Phys. Rev. Lett. **110**, 037402 (2013).

[46] M. Arcari, I. Söllner, A. Javadi, S. Lindskov Hansen, S. Mahmoodian, J. Liu, H. Thyrrestrup, E. H. Lee, J. D. Song, S. Stobbe, and P. Lodahl, Near-unity coupling efficiency of a quantum emitter to a photonic crystal waveguide, Phys. Rev. Lett. **113**, 093603 (2014).

[47] R. Yalla, M. Sadgrove, K. P. Nayak, and K. Hakuta, Cavity quantum electrodynamics on a nanofiber using a composite photonic crystal cavity, Phys. Rev. Lett. **113**, 143601 (2014).

[48] I. Söllner, S. Mahmoodian, S. L. Hansen, L. Midolo, A. Javadi, G. Kiršanskė, T. Pregnolato, H. El-Ella, E. H. Lee, J. D. Song *et al.*, Deterministic photon–emitter coupling in chiral photonic circuits, Nat. Nanotechnol. **10**, 775 (2015).

[49] P. Roushan, C. Neill, A. Megrant, Y. Chen, R. Babbush, R. Barends, B. Campbell, Z. Chen, B. Chiaro, A. Dunsworth *et al.*, Chiral ground-state currents of interacting photons in a synthetic magnetic field, Nat. Phys. **13**, 146 (2017).

[50] D.-W. Wang, C. Song, W. Feng, H. Cai, D. Xu, H. Deng, H. Li, D. Zheng, X. Zhu, H. Wang *et al.*, Synthesis of antisymmetric spin exchange interaction and chiral spin clusters in superconducting circuits, Nat. Phys. **15**, 382 (2019).

[51] C. Sayrin, C. Clausen, B. Albrecht, P. Schneeweiss, and A. Rauschenbeutel, Storage of fiber-guided light in a nanofiber-trapped ensemble of cold atoms, Optica **2**, 353 (2015).

[52] A. Sipahigil, R. E. Evans, D. D. Sukachev, M. J. Burek, J. Borregaard, M. K. Bhaskar, C. T. Nguyen, J. L. Pacheco, H. A. Atikian, C. Meuwly *et al.*, An integrated diamond nanophotonics platform for quantum-optical networks, Science **354**, 847 (2016).

[53] M. K. Bhaskar, D. D. Sukachev, A. Sipahigil, R. E. Evans, M. J. Burek, C. T. Nguyen, L. J. Rogers, P. Siyushev, M. H. Metsch,

H. Park *et al.*, Quantum nonlinear optics with a germanium-vacancy color center in a nanoscale diamond waveguide, Phys. Rev. Lett. **118**, 223603 (2017).

[54] J. Léonard, S. Kim, M. Rispoli, A. Lukin, R. Schittko, J. Kwan, E. Demler, D. Sels, and M. Greiner, Probing the onset of quantum avalanches in a many-body localized system, Nat. Phys. **19**, 481 (2023).

[55] C.-C. Wu, K.-T. Lin, I. G. N. Y. Handayana, C.-H. Chien, S. Goswami, G.-D. Lin, Y.-C. Chen, and H. H. Jen, Atomic excitation delocalization at the clean to disorder interface in a chirally-coupled atomic array, Phys. Rev. Res. **6**, 013159 (2024).

[56] I G. N. Y. Handayana, C.-C. Wu, S. Goswami, Y.-C. Chen, and H. H. Jen, Atomic excitation trapping in dissimilar chirally coupled atomic arrays, Phys. Rev. Res. **6**, 013320 (2024).

[57] R. H. Lehmberg, Radiation from an *N*-atom system. I. General formalism, Phys. Rev. A **2**, 883 (1970).

[58] B. Olmos, C. Liedl, I. Lesanovsky, and P. Schneeweiss, Bragg condition for scattering into a guided optical mode, Phys. Rev. A **104**, 043517 (2021).

[59] A. N. Poddubny, Driven anti-Bragg subradiant correlations in waveguide quantum electrodynamics, Phys. Rev. A **106**, L031702 (2022).

[60] N. C. Murphy, R. Wortis, and W. A. Atkinson, Generalized inverse participation ratio as a possible measure of localization for interacting systems, Phys. Rev. B **83**, 184206 (2011).

[61] P. W. Anderson, More is different, Science **177**, 393 (1972).

[62] S. J. van Enk, Single-particle entanglement, Phys. Rev. A **72**, 064306 (2005).

[63] L.-M. Duan, M. D. Lukin, J. I. Cirac, and P. Zoller, Long-distance quantum communication with atomic ensembles and linear optics, Nature (London) **414**, 413 (2001).

[64] R. Bekenstein, I. Pikovski, H. Pichler, E. Shahmoon, S. F. Yelin, and M. D. Lukin, Quantum metasurfaces with atom arrays, Nat. Phys. **16**, 676 (2020).

[65] C.-H. Chien, S. Goswami, C.-C. Wu, W.-S. Hiew, Y.-C. Chen, and H. H. Jen, Generating graph states in an atom-nanophotonic interface, Quantum Sci. Technol. **9**, 025020 (2024).

[66] A. M. Kaufman, B. J. Lester, and C. A. Regal, Cooling a single atom in an optical tweezer to its quantum ground state, Phys. Rev. X **2**, 041014 (2012).

[67] M. O. Brown, T. Thiele, C. Kiehl, T.-W. Hsu, and C. A. Regal, Gray-molasses optical-tweezer loading: Controlling collisions for scaling atom-array assembly, Phys. Rev. X **9**, 011057 (2019).